ICASSP 2024 - 2024 IEEE International Conference on Acoustics, Speech and Signal Processing (ICASSP) | 979-8-3503-4485-1 /24/$31.00 USG | DOI: 10.1109/ICASSP48485.2024.10446367

LOW OVERHEAD DMG SENSING FOR VITAL SIGNS DETECTION

Steve Blandino[1,2] *Jihoon Bang*[3,4] *Jian Wang*[5] *Samuel Berweger*[6] *Jack Chuang*[5]
Jelena Senic[1,4] *Tanguy Ropitault*[1,2] *Camillo Gentile*[5] *Nada Golmie*[5]

[1] Associate, National Institute of Standards and Technology (NIST), Gaithersburg, MD
[2] Prometheus Computing LLC, Bethesda, MD.
[3] Associate, National Institute of Standards and Technology (NIST), Boulder, CO
[4] University of Colorado, Boulder, CO.
[5] National Institute of Standards and Technology (NIST), Gaithersburg, MD
[6] National Institute of Standards and Technology (NIST), Boulder, CO

ABSTRACT

Sensing biometric markers such as respiration rate (RR) and heart rate (HR) in non-medical contexts using the high resolution of Millimeter-Wave (mmWave) Wi-Fi networks has recently gathered considerable attention. A significant challenge in deploying a Wi-Fi system capable of performing sensing tasks is to minimize the overhead on the communication tasks associated with acquiring sensing information, both in terms radio resources and memory usage. In this paper, we explore the potential of IEEE 802.11bf passive sensing as a means to mitigate overhead, while effectively estimating both RR and HR. We showcase the potential to develop a low overhead Wi-Fi system that precisely captures vital signs, even in demanding situations, such as rapidly increasing RR interfering with HR, by integrating microdoppler processing with super-resolution eigenvector noise subspace analysis. The results shows that the proposed methodology enables RR and HR estimation without any radio-resource overhead and requiring very limited memory usage.

Index Terms— Integrated sensing and communication (ISAC), joint communication and sensing (JCAS), millimeter wave Wi-Fi.

1. INTRODUCTION

Driven by an increasing emphasis on personal well-being and the importance of adopting proactive measures to safeguard health, monitoring of bio-metric markers such as respiration rate (RR) and heart rate (HR), also in non-medical contexts, have gathered considerable attention [1, 2, 3]. The existing methodologies employed to estimate RR and HR often necessitate the utilization of multiple sensors, such as wearable devices[1]. However, these conventional techniques may not be suited for seamless integration into everyday life. In pursuit of more user-friendly and non-intrusive alternatives, many wireless sensing methodologies have been proposed, such as the use of cameras [4] and radars [5].

Recent works in the field of wireless vital signs detection leverage the existing wireless communication infrastructures, such as Wi-Fi systems, [6, 7, 8, 9, 10, 11]. The use of Wi-Fi systems for sensing applications, also known as Wi-Fi Sensing, capitalizes on the widespread deployment and cost-effectiveness of Wi-Fi technology [12]. As a consequence, Task Group IEEE 802.11bf started to work on a Wi-Fi sensing protocol, which supports sensing in frequency bands below 7 GHz, and its mmWave counterpart, the Directional Multi-Gigabit (DMG). DMG sensing [13], exploiting the high directionality of phased antenna arrays and the small antenna sizes that mmWave wavelengths allow, and the large bandwidth for accurate time-of-flight measurements, enables use-cases requiring high spatial resolution, such as RR and HR estimation. Monitoring vital signs using mmWave signals has been investigated in [8, 9, 10], showing experimentally that human vital signs can be accurately monitored.

A significant challenge in deploying a Wi-Fi system that can carry out sensing tasks is to reduce the overhead required to gathering sensing information, in terms of both radio resources and memory usage. When performing sensing tasks, the system may need to allocate a portion of its radio resources to send dedicated sounding sequences or exchange sensing information and feedback, reducing available resources for regular data transmission. Moreover, sensing processing requires the temporary storage of data, such as channel state information (CSI), due to the extended observation time required for achieving finer resolution in the parameter estimation. This can result in increased memory usage and interfere with the conventional Wi-Fi processing. Optimizing a Wi-Fi system for sensing tasks requires managing both the allocation of radio resources and the usage of memory effectively, hence IEEE 802.11bf [14] allows for flexible configurations, offering mainly two distinct operating modes: i) a passive sensing mode that exploits the Wi-Fi beaconing signaling, ensuring sensing capabilities without introducing additional radio resource overhead. ii) an active mode that utilizes a dedicated sensing frame, allowing the channel to be sampled as required to meet specific application requirements. In this paper, we first present the difference between active and passive sensing in IEEE 802.11bf, and we explore passive sensing as a means to limit overhead, while effectively estimating both RR and HR. Moreover, we address the challenge of precisely estimating RR and HR even with reduced sensing observation time. To counteract the reduced resolution resulting from shorter observation time, we combine microdoppler processing with super-resolution eigenvector (EV) noise subspace analysis. To carry out this investigation, we performed real-world measurements using a mmWave phased-array channel sounder that our research group developed[15] .

2. OPERATING MODES OF DMG SENSING

IEEE 802.11bf DMG Sensing refers to the usage of physical layer and medium access control of DMG stations (STAs) to acquire mea-

surements to estimate parameters such as position and velocity of objects. It enables two distinct types of sensing: active and passive sensing.

2.1. Active sensing

In active sensing, sensing physical layer protocol data units (PPDUs) are used to accomplish the sensing task. Active sensing is the most versatile and flexible mode of operation, catering to a wide range of sensing applications. After exchanging the sensing capabilities among participating STAs, the sensing measurements occur via DMG Sensing Instances, grouped into DMG bursts. Each burst forms the sensing observation window and contains two intervals: intra-burst, determining the time between DMG sensing instances, i.e., the pulse repetition interval (PRI), and inter-burst, establishing the sensing application refresh rate, i..e, the frequency of new sensing results acquisition. These measurements are performed using PPDUs that employs training sequences (TRN), enabling a swift angular scan covering multiple directions. Ultimately, the sensing results are reported as required. These reports come in two types: raw results, which include channel state information, and pre-processed sensing results. The pre-processed results provide information either about each individual target, or Doppler-processed results including information about range, velocity, angle of arrival, and angle of departure. Active sensing offers precise parameter control (e.g, PRI, refresh rate), reducing the resources available for communication as it necessitates the use of dedicated sensing PPDUs.

2.2. Passive sensing

Passive sensing empowers STAs to conduct sensing operations solely through the reception of DMG beacon frames transmitted by the Access Point (AP) during its beaconing phase. The AP performs beaconing by iterating over its transmit sector in the Beacon Transmission Interval, which is repeated every Beacon Interval (BI) duration, serving as the PRI from a sensing perspective. Passive sensing enables the AP to convey its sector beam attributes (azimuth, elevation) for sensing processing at the STAs. While passive sensing avoids added overhead by reusing beaconing, its flexibility is constrained by the fixed PRI tied to the BI duration (typically 102.4 ms).

3. MICRODOPPLER SIGNATURES IN DMG SENSING

To gather sensing information, the channel is probed using pilot sequences. In the active sensing mode, TRN are employed for this purpose, while in the passive sensing mode, Channel Estimation Field (CEF) of the preamble may be utilized. Both TRN and CEF contain known complementary Golay sequences. Complementary Golay sequences can be used for channel estimation, hence the same estimation techniques are valid for both active and passive sensing. In this section we provide the steps to obtain microdoppler signatures receiving either DMG beacons or DMG sensing PPDUs.

3.1. Synchronization and channel impulse response estimation

The preamble is used for temporal synchronization between the transmitter and the receiver. To achieve synchronization, the known Short Training Field (STF) is cross-correlated with the received symbols. This process results in a sequence of peaks, and the synchronization is referenced to the delay bin wherein the maximum cross-correlation value is located. The fast-time index of this value corresponds to the propagation delay of the strongest path between the transmitter and receiver. The synchronization point allows to locate the CEF or the TRN, which are thus correlated with the known pair of Golay complementary sequences used in their construction. Using the zero-correlation property of complementary Golay sequences, the output of the correlators can be summed to extract the channel impulse response (CIR) from the zero-correlation zone [16].

3.2. Doppler Processing

In the presence of motion, such as the motion of the chest due to breathing, the CIR exhibits temporal fluctuations due to the phase changes caused by the Doppler shifts. The CIR can be collected over different angles, using beamforming techniques, and over different time instances (the interval separating the time instances depends from the mode: it is configurable for the active sensing mode and fixed to the BI for the passive sensing mode). The result is the three dimensional (3D) sensing data matrix, including time, delay and angle domains. The angle dimension can be used to distinguish various targets, as shown in [8, 9, 11]. However, without losing generality, we make the assumption of a single target scenario, so that a 2D matrix is sufficient for our analysis. M CIR estimations of length N delay samples, are collected by sampling the channel at regular intervals, obtaining the 2D sensing data matrix $\mathbf{H} = [\widehat{\mathbf{h}}_1, \widehat{\mathbf{h}}_2 \cdots, \widehat{\mathbf{h}}_M]$, where $\mathbf{h}_m \in \mathbb{C}^{N\times 1}$ contains the CIR estimate at time m.

To analyze how the frequency content of the signal changes over time we compute range-Doppler maps using the Short-time Fourier Transform (STFT). A discrete Fourier transform (DFT) is applied to each segment of the windowed data matrix by using the window $\mathbf{w}$ of length W_L. The window hops over the original matrix at intervals of W_H samples. The DFT is applied to each delay bin k along the time dimension of the sensing data matrix to obtain the Doppler matrix, $\mathbf{D}^s[k,\nu] = \sum_{m=1}^{W_L} \widehat{h}_{(m+sW_H)}[k] w(m) \exp(-j2\pi m T_M \nu / N_\nu)$, where ν is the Doppler bin index, N_ν is the DFT size and T_M is the PRI, which correspond to the DMG Intra-burst interval in active sensing and to the BI in passive sensing. The integer index $s = 0, 1, \ldots, L$ indicates the segment over which the DFT is computed and $L = \lfloor \frac{M-W_L}{W_H} \rfloor$. The range-Doppler maps can be used to compute the microdoppler signal created by rhythmic movements of body parts, which include the movement of chest and abdomen walls due to the cardiac and respiratory cycles.

3.3. Chest velocity estimation

To locate the human target, our first step involves identifying the range-Doppler bins that contain the scattered signals from the chest. In this work we utilize a cell-average constant false-alarm rate (CFAR) detector. The CFAR detector works by estimating the background noise level and comparing the signal power in each bin to the estimated noise power. The power of the noise level for the cell under test (CUT), $P_N^s[k,\nu]$, is estimated by averaging the power of the surrounding training cells, i.e., $P_N^s[k,\nu] = \frac{1}{N_T} \sum_p \sum_q |\mathbf{D}^s[k+p, \nu+q]|^2$, $\forall (p,k) \in T$ where T is the set of training cells of cardinality $|T| = N_T$. A scaling factor α is applied to scale the estimated noise level, such that the detection threshold is set to $\gamma^s[k,\nu] = \alpha P_N^s[k,\nu]$. The value of $\mathbf{D}^s[k,\nu]^2$ must be above the detection threshold to be classified as detection, i.e., $\hat{\mathbf{D}}^s[k,\nu] = \mathbf{D}^s[k,\nu]$, if $\mathbf{D}^s[k,\nu]^2 > \gamma^s[k,\nu]$ and $\hat{\mathbf{D}}^s[k,\nu] = 0$, if $\mathbf{D}^s[k,\nu]^2 \leq \gamma^s[k,\nu]$.

To obtain the velocity estimation, the range-Doppler CFAR detections $\hat{\mathbf{D}}^s$ are summed over the range dimension, obtaining

the micro-Doppler spectrum as $\mu\mathbf{D}^s[\nu] = \sum_k \widehat{\mathbf{D}}^s[k,\nu]$. The point with the highest intensity in the micro-Doppler spectrum $\nu^s = \text{argmax}_\nu(\mu\mathbf{D}^s)$ is the estimated Doppler shift. The velocity can be obtained as $v^s = \nu^s c/f_c$, where c and f_c denote the speed of light and carrier frequency, respectively. The velocity over time is thus obtained by resampling the L velocity estimates to obtain $\mathbf{v} = [v^1, v^2, \ldots, v^M]^T$.

4. VITAL SIGNS FREQUENCY ESTIMATION

By analyzing the frequency components of $\mathbf{v}$ and determining the frequency of the chest and heart's motion, RR and HR can be estimated. We utilize two methods to get the spectral representation of the chest velocity. First, we use conventional Fourier spectrum analysis, that requires an integration time of W seconds to obtain a frequency resolution of $f = (60/W)$ beats per minute (BPM). Therefore, to get an acceptable estimation accuracy of the RR and HR, the integration time should be long enough, which will cause a large overhead both in terms of memory and also, in the case of active sensing, of radio resources. The limitations of the classical processing methods can be addressed using noise subspace frequency estimators.

4.1. Welch's spectrogram

For our first method to improve the statistical stability of the classical spectrogram estimators, pseudo ensemble averaging over data segments are used. We employ Welch's spectrogram method to analyze the power spectral density of $\mathbf{v}$ [17]. We start by splitting the velocity estimate, $\mathbf{v}$, into P overlapping segments of length N_p, such that the p-th segment is $\mathbf{v}(p) = [v_p \ldots v_{(p+N_p-1)}]$ and $P = M - N_p + 1$. Each segment is windowed with a discrete window function, before computing the periodogram. The periodogram estimate of the power spectral density thus is given by $P_{\text{Welch}}[k] = \frac{1}{P}\sum_{p=1}^{P} |V_p[k]|^2$, where $V_p[k]$ is the Fourier Transform of the p-th windowed segment.

4.2. Eigenvector noise subspace pseudo-spectrogram

It is desirable to be able to acquire HR and RR using as few data points as possible, hence reducing the overhead involved in transmitting sensing pilots and/or storing in memory the data required for the sensing processing. In our second method, we employ the eigenvector (EV) algorithm, which is a noise subspace-based method that requires the eigenvalue decomposition of the sample covariance matrix of the signal $\mathbf{v}$ [18, 19].

Since a single measurement of $\mathbf{v}$ of length M is available, the data sequence is divided into P consecutive segments of length N_p, as for Welch's method, and then the correlation matrix is estimated as $\hat{\mathbf{R}}_{vv} = \frac{1}{P}\sum_{p=1}^{P} \mathbf{v}(p)\mathbf{v}(p)^H$. However, the estimate of the correlation matrix $\hat{\mathbf{R}}_{vv}$, based on the actual sample data of small finite length, is not Toeplitz. The estimate of the correlation matrix can be improved using the forward–backward correlation matrix (FBCM) $\hat{\mathbf{R}}_{vv}^{FB} = \frac{1}{2}(\hat{\mathbf{R}}_{vv} + \mathbf{J}\hat{\mathbf{R}}^*_{vv}\mathbf{J})$, where the superscript * denotes conjugate and $\mathbf{J}$ is the exchange matrix whose components are zero except for ones on the antidiagonal, so that $\mathbf{J} = \mathbf{J}^H$. The eigenvalue decomposition of the FBCM is $\hat{\mathbf{R}}_{vv}^{FB} = \mathbf{U}\mathbf{\Lambda}\mathbf{U}^H$, where the matrix $\mathbf{U} \in \mathbb{C}^{N_p \times N_p}$ includes the eigenvectors $\mathbf{u_1}, \ldots, \mathbf{u}_{N_p}$ spanning signal and noise subspace and $\mathbf{\Lambda}$ is the diagonal matrix including the corresponding eigvalues $\lambda_1 \ldots \lambda_{N_p}$. The eigenvectors corresponding to the largest Q eigenvalues are the signal eigenvectors. The eigenvectors corresponding to the smallest $N_p - Q$ eigenvalues are the noise eigenvectors that construct the noise space E_N. The pseudo spectrum estimate is obtained from the noise estimate as $P_{\text{EV}} = 1/\left(\sum_{i=Q+1}^{N_p} \frac{1}{\lambda_i}|\mathbf{u}_i^H\mathbf{a}|^2\right)$, where $\mathbf{a}$ is a vector of complex sinusoids, so the inner product $\mathbf{u}_i^H\mathbf{a}$ is the equivalent to a Fourier transform of $\mathbf{u}$.

5. ESTIMATING VITAL SIGNS USING MMWAVE PHASED ARRAY CHANNEL SOUNDER

In this section, we present a comprehensive evaluation methodology that includes a measurement campaign, the extraction of the channel Multipath Components (MPCs), and subsequent simulations of a DMG transmission. Through this methodology, we derive vital signs with a focus on minimizing the sensing overhead.

5.1. mmWave channel measurements

We carried out a measurement campaign with a mmWave phased-antenna array channel sounder, developed by our research group at NIST [15]. The channel sounder operates at a center frequency of 28.5 GHz. A repeated M-ary pseudorandom-noise (PN) code of 2047 chips with 0.5 ns chip duration is used for sensing. The system transmits at 2 Gb/s with an oversampling factor of 8. The measurement campaign adopts a quasi mono-static deployment, and the transmitter has a phased antenna array with 64 elements, while the receiver employs a phased antenna array with 256 elements. In the measurement campaign, the channel was sampled at a time interval of 26 ms. The human target is sitting at 2.5 m away from the assembly containing the transmitter and receiver. To extract the MPCs from the receive waveform, the CLEAN algorithm was combined with a least square power estimation technique [20].

5.2. Microdoppler in DMG sensing

We use the extracted MPCs to simulate a DMG sensing transmission, using NIST ISAC-PLM, an open-source implementation of the DMG physical layer of the IEEE 802.11bf, developed by our research group at NIST [21, 22]. The microdoppler signatures are generated using $M = 960$ packets in active sensing mode, sounding the channel at $T_M = 26$ ms, while in passive sensing mode we use $M = 240$, sounding the channel at $T_M = 104$ ms (which closely resembles the BI). STFT processing was applied using a Hamming window of length $W_L = 32$ in active sensing and $W_L = 8$ in passive sensing, to keep a total integration time of $T_M W_L = 0.832$ s. The DFT length is set to $N_\nu = 256$ and $N_\nu = 64$ in active and passive sensing respectively, to provide a velocity resolution of 0.37 mm/s. The window overlap is set to 90 %, i.e., $W_H = 4$ and $W_H = 1$ in active and passive sensing respectively. The Signal-to-Noise ratio (SNR) was assumed to be 0 dB.

Active sensing coherently combines more data packets than passive sensing, thus achieving a greater integration gain in SNR, hence providing greater resilience to noise, enhancing the overall robustness of the microdoppler map. For this reason, the design of the CFAR is influenced by the sensing mode. In the case of active sensing, a CFAR threshold of $\alpha = 6$ dB is determined to be suitable. In contrast, the optimal CFAR threshold for passive sensing is lowered to $\alpha = 2$ dB. Fig. 1 shows the microdoppler signatures obtained with the two sensing modes. The microdoppler obtained in active sensing mode, shown in Fig. 1a, highlights the advantages of a faster channel sounding, resulting in a less noisy signature compared to the passive mode shown in Fig. 1b. Even in low SNR regime, thanks to the integration gain, in both cases the target is detected and the velocity $\mathbf{v}$ is estimated.

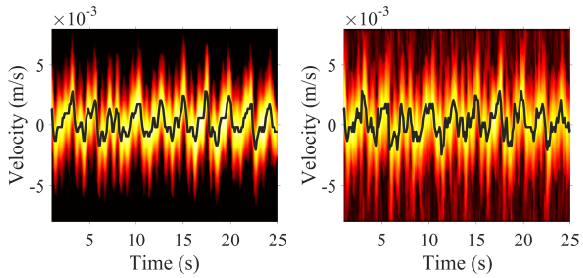

(a) Active sensing, $M = 960$. (b) Passive sensing, $M = 240$.

Fig. 1: Velocity estimation with micro-doppler processing.

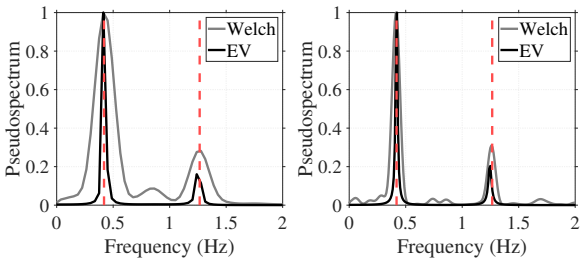

(a) Active sensing, $M = 960$. (b) Passive sensing, $M = 240$.

Fig. 2: Pseudo-spectrum of the chest velocity estimate.

5.3. Vital Sign Estimation

After the target detection and the velocity estimation, we investigate the microdoppler frequency content. For evaluating our proposed methodology, RR and HR are verified using external instrumentation, i.e., a chest strap equipped with an accelerometer for measuring the chest compression frequency and an ECG sensor for capturing the HR of the subject. The ground truth RR is derived filtering the accelerometer output with a second order lowpass Butterworth filter and performing peaks detection to find the breath cycles, yielding as estimation $f_R = 0.42$ Hz. The ground truth HR is derived using the Pan-Tompkins algorithm on the ECG sensor data [23], yielding as estimation $f_H = 1.27$ Hz. Throughout the section, using EV, $Q = 4$ represents the signal subspace; $N_p = 92$ and $N_p = 23$ in active and passive mode respectively. Using Welch, $N_p = 2M/3$.

In the first experiment, we compare the spectra obtained with active sensing and passive sensing, from a capture time of 25 s. Fig. 2, shows the frequency spectrum of the microdoppler obtained with active sensing and passive sensing, using both Welch and EV. In active sensing (Fig. 2a), we observe the presence of two prominent peaks at $\hat{f}_R = 0.41$ Hz and $\hat{f}_H = 1.28$ Hz using Welch processing, and $\hat{f}_R = 0.41$ Hz and $\hat{f}_H = 1.25$ Hz using the EV method. The estimated frequencies align closely with the f_R and f_H. Similar results are obtained using passive sensing (Fig. 2b). The similarity in the spectral peaks observed using both active and passive sensing modalities underscores the potential of passive sensing using existing BI sounding; hence, non-intrusive physiological monitoring can be obtained without incurring in communication overhead.

To minimize overhead, including radio resources and memory usage, we explored the effects of minimizing the collection time by sounding the channel with $M = 512$ packets in active sensing mode and $M = 128$ in passive sensing mode, generating 5 s of chest velocity estimate. Fig. 3 shows that even with the substantial reduction of velocity estimation, both Welch and EV continue to successfully reproduce the HR and RR peaks in both active sensing (Fig. 3a) and passive sensing modes (Fig. 3b).

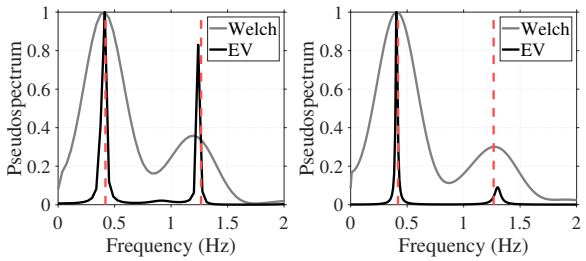

(a) Active Sensing, $M = 192$. (b) Passive Sensing, $M = 48$.

Fig. 3: Pseudo-spectrum of the chest velocity estimate.

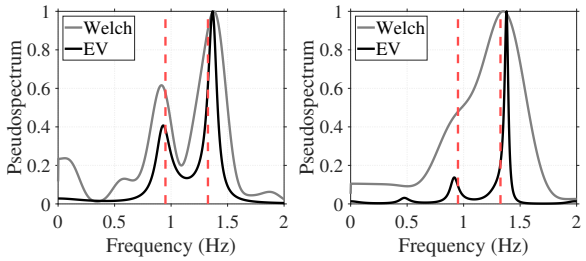

(a) Passive sensing, $M = 96$. (b) Passive sensing, $M = 48$.

Fig. 4: Pseudo-spectrum of chest velocity estimate of a subject instructed to engage in rapid breathing.

To assess the robustness of the vital signs detection we conduct an experiment where the subject is instructed to engage in rapid breathing, emulating the need of identifying potential health conditions such as Tachypnea, i.e. abnormally fast breathing. The aim is to evaluate whether passive sensing could reliably detect such conditions even with a limited observation time. While sensing with $M = 96$ packets (Fig. 4a) Welch processing is still able to capture both RR and RR, reducing the overhead even more to $M = 48$ (Fig. 4b), the results indicate a significant difference in performance between Welch and EV techniques. The two peaks collapse into a single peak using Welch processing, in contrast, the EV method exhibited greater robustness, continuing to successfully identify both the RR and HR peaks.

6. CONCLUSION

This paper provides a methodology to estimate biometric markers such as RR and HR using DMG sensing. The microdoppler processing provides robustness thanks to the integration gain enabling the estimation of the chest motion in low SNR regime. We demonstrate that passive sensing can effectively be used to estimate both RR and HR, avoiding any radio-resources overhead. To minimize also memory usage, we show that the HR and RR can be effectively extracted while reducing the number of processed packets. In more challenging scenarios, such in situations with rapidly increasing RR, super-resolution techniques, such as the EV method, can reconstruct the power spectrum of the microdoppler indicating the viability of a low overhead mmWave Wi-Fi system for early identification of physiological abnormalities, even with short observation times.

7. REFERENCES

[1] Andriy Temko, "Accurate heart rate monitoring during physical exercises using PPG," *IEEE Transactions on Biomedical Engineering*, vol. 64, no. 9, pp. 2016–2024, 2017.

[2] Hye-Geum Kim, Eun-Jin Cheon, Dai-Seg Bai, Young Hwan Lee, and Bon-Hoon Koo, "Stress and heart rate variability: a meta-analysis and review of the literature," *Psychiatry investigation*, vol. 15, no. 3, pp. 235, 2018.

[3] Jian Wang, Neeraj Varshney, Camillo Gentile, Steve Blandino, Jack Chuang, and Nada Golmie, "Integrated sensing and communication: Enabling techniques, applications, tools and data sets, standardization, and future directions," *IEEE Internet of Things Journal*, vol. 9, no. 23, pp. 23416–23440, 2022.

[4] Guha Balakrishnan, Fredo Durand, and John Guttag, "Detecting pulse from head motions in video," in *2013 IEEE Conference on Computer Vision and Pattern Recognition*, 2013, pp. 3430–3437.

[5] Akshay Visweswaran, Kristof Vaesen, Miguel Glassee, Anirudh Kankuppe, Siddhartha Sinha, Claude Desset, Thomas Gielen, Andre Bourdoux, and Piet Wambacq, "A 28-nm-CMOS based 145-GHz FMCW radar: System, circuits, and characterization," *IEEE Journal of Solid-State Circuits*, vol. 56, no. 7, pp. 1975–1993, 2021.

[6] Fadel Adib, Hongzi Mao, Zachary Kabelac, Dina Katabi, and Robert C. Miller, "Smart homes that monitor breathing and heart rate," in *Proceedings of the 33rd Annual ACM Conference on Human Factors in Computing Systems*, New York, NY, USA, 2015, CHI '15, p. 837–846, Association for Computing Machinery.

[7] Susanna Mosleh, Jason B. Coder, Christopher G. Scully, Keith Forsyth, and Mohamad Omar Al Kalaa, "Monitoring respiratory motion with Wi-Fi CSI: Characterizing performance and the breathesmart algorithm," *IEEE Access*, vol. 10, pp. 131932–131951, 2022.

[8] Fengyu Wang, Feng Zhang, Chenshu Wu, Beibei Wang, and K. J. Ray Liu, "ViMo: Vital sign monitoring using commodity millimeter wave radio," in *ICASSP 2020 - 2020 IEEE International Conference on Acoustics, Speech and Signal Processing (ICASSP)*, 2020, pp. 8304–8308.

[9] Fengyu Wang, Feng Zhang, Chenshu Wu, Beibei Wang, and K. J. Ray Liu, "ViMo: Multiperson vital sign monitoring using commodity millimeter-wave radio," *IEEE Internet of Things Journal*, vol. 8, no. 3, pp. 1294–1307, 2021.

[10] Zhicheng Yang, Parth H. Pathak, Yunze Zeng, Xixi Liran, and Prasant Mohapatra, "Monitoring vital signs using millimeter wave," in *Proceedings of the 17th ACM International Symposium on Mobile Ad Hoc Networking and Computing*, New York, NY, USA, 2016, MobiHoc '16, p. 211–220, Association for Computing Machinery.

[11] Haoqiu Xiong, Zhuangzhuang Cui, Mingqing Liu, Yang Miao, and Sofie Pollin, "Multi-person localization and respiration sensing under IEEE 802.11ay standard," in *Proceedings of the 3rd ACM MobiCom Workshop on Integrated Sensing and Communications Systems*, New York, NY, USA, 2023, ISACom '23, p. 31–36, Association for Computing Machinery.

[12] Tanguy Ropitault, Steve Blandino, Anirudha Sahoo, and Nada T Golmie, "IEEE 802.11 bf: Enabling the widespread adoption of Wi-Fi sensing," *IEEE Communications Standards Magazine*, 2023.

[13] Steve Blandino, Tanguy Ropitault, Claudio R. C. M. da Silva, Anirudha Sahoo, and Nada Golmie, "IEEE 802.11bf DMG sensing: Enabling high-resolution mmWave Wi-Fi sensing," *IEEE Open Journal of Vehicular Technology*, vol. 4, pp. 342–355, 2023.

[14] "IEEE P802.11bf™/D2.0 draft standard for information technology— telecommunications and information exchange between systems local and metropolitan area networks— specific requirements part 11: Wireless LAN medium access control (MAC) and physical layer (PHY) specifications amendment 2: Enhancements for wireless LAN sensing," 2023.

[15] Derek Caudill, Jack Chuang, Sung Yun Jun, Camillo Gentile, and Nada Golmie, "Real-time mmWave channel sounding through switched beamforming with 3-D dual-polarized phased-array antennas," *IEEE Transactions on Microwave Theory and Techniques*, vol. 69, no. 11, pp. 5021–5032, 2021.

[16] François Horlin and André Bourdoux, *Digital compensation for analog front-ends: a new approach to wireless transceiver design*, John Wiley & Sons, 2008.

[17] S Lawrence Marple Jr, *Digital spectral analysis*, Courier Dover Publications, 2019.

[18] Xinrong Li and K. Pahlavan, "Super-resolution TOA estimation with diversity for indoor geolocation," *IEEE Transactions on Wireless Communications*, vol. 3, no. 1, pp. 224–234, 2004.

[19] Jian Wang, Jack Chuang, Samuel Berweger, Camillo Gentile, and Nada Golmie, "Towards opportunistic radar sensing using millimeter-wave Wi-Fi," *IEEE Internet of Things Journal*, pp. 1–1, 2023.

[20] JA Högbom, "Aperture synthesis with a non-regular distribution of interferometer baselines," *Astronomy and Astrophysics Supplement, Vol. 15, p. 417*, vol. 15, pp. 417, 1974.

[21] Steve Blandino, Tanguy Ropitault, Anirudha Sahoo, and Nada Golmie, "Tools, models and dataset for IEEE 802.11ay CSI-based sensing," in *2022 IEEE Wireless Communications and Networking Conference (WCNC)*, 2022, pp. 662–667.

[22] National Institute of Standard and Technology, "Integrated Sensing and Communication Physical Layer Model," `https://github.com/wigig-tools/isac-plm`.

[23] Jiapu Pan and Willis J. Tompkins, "A real-time QRS detection algorithm," *IEEE Transactions on Biomedical Engineering*, vol. BME-32, no. 3, pp. 230–236, 1985.